Climate Dynamics
https://doi.org/10.1007/s00382-018-4433-7

Dynamic moisture mode versus moisture mode in MJO dynamics: importance of the wave feedback and boundary layer convergence feedback

Guosen Chen[1,2] · **Bin Wang**[1,2]

Received: 6 March 2018 / Accepted: 6 September 2018
© The Author(s) 2018

Abstract
The Madden–Julian oscillation (MJO) is an equatorial eastward moving system with a planetary-scale coupled Kelvin–Rossby wave structure. The equatorial waves and their interaction with convection are expected to play an important role in MJO dynamics. Using the trio-interaction model for essential MJO dynamics, this study investigates the importance of dynamic feedback that includes wave feedback (WF) and boundary layer convergence feedback (BLCF), by comparing the moisture mode (MM) that contains only moisture feedback (MF) and cloud-radiative feedback (CRF), with the dynamic moisture mode (DMM) that includes additional WF and BLCF. It is shown that the dynamic feedbacks fundamentally change the properties of the MJO mode. For the MM, the MF alone yields a damping and quasi-stationary mode on wavenumber 2–4. The CRF can destabilize the MM, but it cannot produce planetary wave selection. By including the dynamic feedbacks (WF and BLCF), the resultant DMM is an unstable mode with a preferred planetary scale, which moves eastward slowly, yielding a 30–90-day period. The dynamic feedbacks produce the planetary scale selection of the DMM through generating more eddy available moist static energy on the longer wavelengths. The WF can significantly change the structure of the MM and links the propagation of the DMM to the Kelvin and Rossby wave components, with stronger Kelvin (Rossby) wave favoring faster (slower) propagation. The BLCF enhances the Kelvin wave component on the longer wavelengths, changing the horizontal structures and accelerating the eastward propagation. The WF relates the dispersion feature of the DMM to the properties of the Kelvin and Rossby waves. Since the Kelvin-wave (Rossby-wave) frequency increases (decreases) with increasing wavenumber, their coupling in the DMM yields a quasi-constant frequency at the planetary scales (wavenumber 1–3).

Keywords MJO theory · Moisture mode · Dynamic moisture mode · Moisture feedback · Cloud-radiation feedback · Wave feedback · Boundary layer convergence feedback

1 Introduction

The Madden–Julian oscillation (MJO) (Madden and Julian 1971, 1972) is a convectively coupled, planetary scale circulation system (Madden and Julian 1972) which propagates eastward slowly with a speed of about 3–6 m/s over the warm-pool ocean (Knutson et al. 1986; Zhang and Ling 2017) and consequently has a period of 30–90 days (Zhang 2005). Understanding the fundamental dynamics of the MJO is the "holy grail" in the study of tropical dynamics (Raymond 2001).

On the wavenumber–frequency spectra diagram of Outgoing Longwave Radiation (OLR), the MJO dominates the tropical variability and displays the strongest signals on planetary scales (Wheeler and Kiladis 1999; Hendon and Wheeler 2008); it also has a peculiar dispersion relation ($\partial w/\partial k \approx 0$) which differs from those of the theoretical equatorial waves (Matsuno 1966). To illustrate the unique wavenumber–frequency characteristics of MJO precipitation, we show, in Fig. 1, the observed wavenumber–frequency power spectra of the daily precipitation data, which are normalized by the background spectra following Wheeler and Kiladis (1999). Evidently, the MJO signals are concentrated on

✉ Guosen Chen
chenguos@hawaii.edu

[1] Earth System Modeling Center, Nanjing University of Information Science and Technology, Nanjing, China

[2] Department of Atmospheric Sciences and Atmosphere-Ocean Research Center, University of Hawaii at Manoa, Honolulu, HI 96822, USA

Published online: 14 September 2018

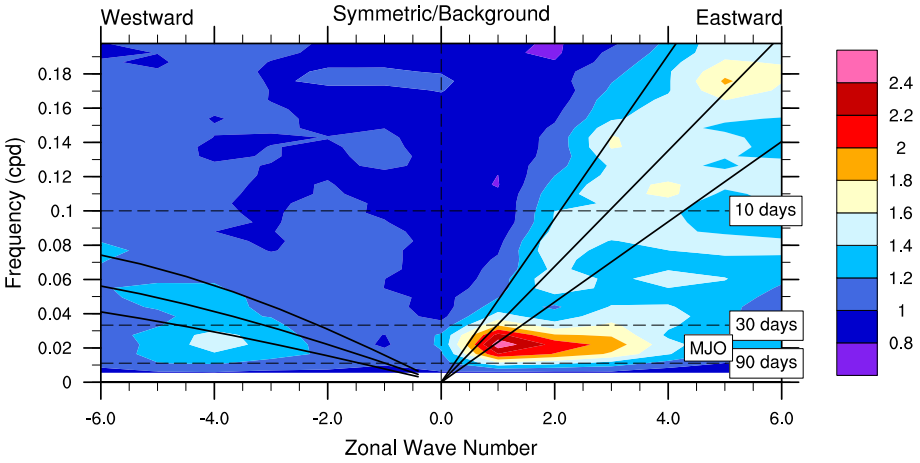

Fig. 1 Observed wavenumber–frequency power spectra of the daily precipitation data, normalized by the background spectra following Wheeler and Kiladis (1999). Superimposed are the dispersion curves of the equatorial waves for the three equivalent depths of 12, 25, and 50 m. The precipitation data used is the daily accumulated precipitation (mm) from the 3B42 version 7 product of the Tropical Rainfall Measuring Mission (TRMM-3B42) (Huffman et al. 2007), based on the period of record from 1998 to 2016

the planetary scales (wavenumber 1–3) with a maximum at wavenumber one, suggesting a preferred zonal planetary scale. It is noted that the MJO frequency is nearly independent of the wavenumber, indicating a near zero group velocity ($\frac{\partial \omega}{\partial k} \approx 0$) (Chen and Wang 2018).

Theoretical models are capable of elucidating fundamental dynamics of the MJO by containing only essential physical processes. Wang and Chen (2017) and Wang et al. (2016) proposed a theoretical trio-interaction model for the study of essential MJO dynamics, which includes the key elements of large-scale MJO dynamics in many major existing MJO theories. This trio-interaction framework, as shown in Fig. 2, involves an active interaction among convective heating, moisture and dynamics. In this framework, convective heating contains precipitation heating and the cloud-radiation feedback (CRF); the moisture process comprises a time-dependent moisture budget and the associated moisture feedback (MF); the dynamics include the free atmospheric wave dynamics and the associated wave feedback (WF), along with the boundary layer (BL) dynamics and the associated BL convergence feedback (BLCF). The WF, which is manifested in the prognostic equations of momentum and thermodynamics, is the feedback of wave propagation to moisture and convection fields. The MF, which is manifested through inclusion of a prognostic moisture equation (with the moisture tendency retained) and a simplified convective parameterization, is the feedback of the change of moisture to convection.

In early MJO theories (Emanuel 1987; Lau and Peng 1987; Neelin et al. 1987; Wang 1988; Wang and Rui 1990a; Wang and Li 1994), the interaction between convective heating and wave dynamics is emphasized, while the MF is overlooked. The framework of this group of MJO theories

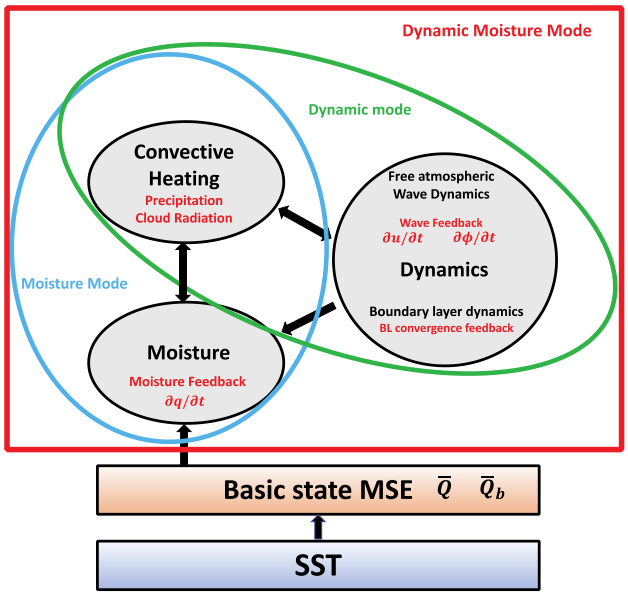

Fig. 2 Schematic diagram of the MJO trio-interaction theoretical framework (Wang et al. 2016). The blue oval outlines the framework of the moisture mode, the green oval outlines the framework of the dynamic mode and the red rectangular outlines the framework of the dynamic moisture mode

falls in the regime encircled by the green oval in Fig. 2. The MJO-mode in this regime can be regarded as a dynamic mode as this mode mainly involves the wave-BL dynamics and their interactions with convective heating.

Recognizing the importance of moisture feedback processes (Benedict and Randall 2007, Hsu and Li 2012; Feng et al. 2015; Johnson et al. 2015), there is a growing body of theories that emphasize the interaction between moisture

and convection by incorporating the MF. Among them, the "moisture mode" theory (Sobel and Maloney 2012, 2013; Adames and Kim 2016) considers moisture anomaly as the only prognostic variable, thereby emphasizing the importance of the MF while it neglects the WF by using diagnostic momentum and thermodynamic equations. The framework of this group of MJO theories falls in the regime encircled by the blue oval in Fig. 2. The associated moisture mode (MM) can be regarded as a thermodynamic mode, since it mainly consists of the thermodynamic processes associated with the interaction between moisture and convection.

Besides, there exists a third group of MJO theories that contains ingredients of both the moisture and dynamic feedbacks (Raymond 2001; Fuchs and Raymond 2005, 2017; Majda and Stechmann 2009; Liu and Wang 2012, 2016, 2017; Wang et al. 2016; Wang and Chen 2017). The work of Wang and Chen (2017) provided a comprehensive theoretical framework which includes a variety of simplified convective parameterization schemes and both the dynamic feedback (WF and BLCF) and thermodynamic feedback (MF and CRF) processes. The general framework of this group of MJO theories falls in the regime outlined by the red rectangle in Fig. 2. The associated MJO mode can be regarded as a dynamic moisture mode (DMM).

Since the MJO has a coupled Kelvin–Rossby wave structure (Wang and Rui 1990b; Hendon and Salby 1994; Maloney and Hartmann 1998; Matthews 2000; Adames and Wallace 2014; Wang and Lee 2017), the equatorial waves and their interaction with convection are arguably important for MJO dynamics. It is interesting to examine the difference between the MM and DMM or study how adding dynamic feedbacks (WF and BLCF) change properties of the MM. Liu and Wang (2017) recently compared the MJO-like modes with and without the WF in the presence of BLCF, and found marked differences in the eastward propagation, instability, horizontal structures and dispersion relation. However, the mechanisms responsible for these differences remain elusive. Specifically, it is uncertain whether the eastward propagation and wave selection mechanisms are different between the MJO modes with and without the WF.

To address these questions, we will use the MJO trio-interaction model (Wang and Chen 2017) to conduct a linear normal mode analysis. With a simplified Betts–Miller convection scheme, this trio-interaction model has been shown to be able to reproduce a number of key large-scale characteristics of the observed MJO (Liu and Wang 2016, 2017; Wang et al. 2016; Chen and Wang 2017; Wang and Chen 2017), thereby establishing its credibility in studying the issues raised here.

Besides the WF, the MF and parameterized precipitation, two additional physical processes are included in this study. One is the BLCF, which is the feedback of BL convergence to moisture and convection fields. The BLCF has been considered important for the MJO's eastward propagation and unstable growth in both observational studies (Hendon and Salby 1994; Benedict and Randall 2007, Hsu and Li 2012; Wang and Lee 2017) and theoretical studies (Wang and Rui 1990a; Wang and Li 1994; Liu and Wang 2016; Wang et al. 2016; Wang and Chen 2017). The other process is the CRF, which is the reduction of longwave radiation cooling due to the presence of deep convection. The CRF not only provides instability for the growth and maintenance of the MJO (Raymond 2001; Bony and Emanuel 2005; Fuchs and Raymond 2005; Andersen and Kuang 2012; Arnold et al. 2013; Sobel and Maloney 2013; Adames and Kim 2016) but also slows down its eastward propagation (Bony and Emanuel 2005; Andersen and Kuang 2012; Crueger and Stevens 2015).

The purpose of this study is to investigate the dynamical differences between the MM and the DMM of the MJO dynamics in a linear system, and to understand how different feedback processes, especially the dynamic feedbacks (the WF and the BLCF), affect the eastward propagation, instability, circulation structures and dispersion relation. The rest of the paper is structured as follows. Section 2 describes the trio-interaction model framework and the linear eigenvalue technique. Sections 3 and 4 explore the characteristic features of the MM and DMM, respectively. In Sect. 5, the mechanisms responsible for the differences between the MM and DMM are elaborated. Conclusion and discussion are presented in Sect. 6.

2 The model and methods

2.1 The general MJO theoretical framework

Wang and Chen (2017) proposed a general theoretical framework for studying the fundamental dynamics of the MJO. The model framework is a 1 and 1/2 layer equatorial beta-plane model, which depicts the first baroclinic mode in the free troposphere and the barotropic BL dynamics (Wang 1988). Detailed derivation of the model equations is given in Wang and Chen (2017). Briefly, the linearized non-dimensional governing equations are:

$$\left(\frac{\partial}{\partial t}+\varepsilon\right)u - yv = -\frac{\partial \Phi}{\partial x} \tag{1}$$

$$yu = -\frac{\partial \Phi}{\partial y} \tag{2}$$

$$\left(\frac{\partial}{\partial t}+\varepsilon\right)\Phi + \frac{\partial u}{\partial x} + \frac{\partial v}{\partial y} = -dD_b - Pr - R \tag{3}$$

$$\frac{\partial q}{\partial t} + \bar{Q}\left(\frac{\partial u}{\partial x} + \frac{\partial v}{\partial y}\right) + d\bar{Q}_b D_b = -Pr \tag{4}$$

Here, the horizontal velocity scale is $C_0 = 50\ m/s$ (gravity wave speed in a dry atmosphere), the length scale is $L = \left(C_0/\beta\right)^{1/2}$, the time scale is $T_0 = \left(\beta C_0\right)^{-1/2}$, the geopotential scale is C_0^2 and the moisture scale is q_{ref} (see Table 1 for q_{ref}).

Equations (1–2) are the zonal and meridional momentum equations. Equation (3) is the combined hydrostatic, continuity and thermodynamic equation. u, v and Φ represent the free-tropospheric low-level zonal wind, meridional wind and geopotential of the first baroclinic mode, respectively. Since the observed zonal scale of the MJO is much larger than its meridional scale, the long wave approximation in Eqs. (1–3), which neglects the time tendency of the meridional wind, can be obtained by using scaling analysis and perturbation method (Ogrosky and Stechmann 2015). $d = 0.25$ is the nondimensional BL depth. D_b is BL divergence. ε represents the longwave Newtonian cooling and Rayleigh friction coefficients. Pr and R are the precipitation rate and cloud radiation, respectively. Surface evaporation is neglected, but its inclusion is trivial.

Equation (4) is the vertically integrated moisture equation. q is the column-integrated specific humidity anomaly from surface to tropopause. $\bar{Q}$, the difference of normalized basic-state specific humidity between the lower and upper layer, represents the moisture stratification of the middle atmosphere; $\bar{Q}_b$, the difference of normalized basic-state specific humidity between the BL and the upper layer, represents the moisture stratification of the whole troposphere. The definitions of $\bar{Q}$ and $\bar{Q}_b$ here are slightly different from those in Wang and Chen (2017), in which the upper-level basic-state specific humidity was neglected. Readers are referred to "Appendix" for more details. $\bar{Q}$ and $\bar{Q}_b$ are constants and controlled by the underlying sea surface temperature (SST) (Wang and Li 1994; Wang and Chen 2017). The SST is set to 28.5 °C in this study unless otherwise specified.

Since the Ekman coefficient (damping in BL) is large, the BL flow adjusts very fast to the quasi-steady state and it has much shorter time scale compared to that of the MJO. Therefore, a stationary BL can be used in this study (Wang and Rui 1990a):

$$-yv_b = -\frac{\partial \Phi}{\partial x} - Eu_b \tag{5}$$

$$yu_b = -\frac{\partial \Phi}{\partial y} - Ev_b \tag{6}$$

where the variables with subscript b represent the variables in BL. The BL divergence in this stationary BL can be expressed as (Wang and Rui 1990a):

$$\begin{aligned} D_b = \frac{\partial u_b}{\partial x} + \frac{\partial v_b}{\partial y} = -\frac{E}{E^2 + y^2}\left(\frac{\partial^2 \Phi}{\partial x^2} + \frac{\partial^2 \Phi}{\partial y^2}\right) \\ + \frac{E^2 - y^2}{\left(E^2 + y^2\right)^2}\frac{\partial \Phi}{\partial x} + \frac{2Ey}{\left(E^2 + y^2\right)^2}\frac{\partial \Phi}{\partial y} \end{aligned} \tag{7}$$

2.2 Parameterization

2.2.1 Precipitation

The properties of the MJO mode in the trio-interaction model depend on the forms of cumulus parameterization (Wang et al. 2016). To facilitate comparison, the parameterization of precipitation anomaly in this study follows Bretherton et al. (2004):

$$Pr = \frac{q}{\tau} \tag{8}$$

where τ is the convective relaxation time (τ is set to 12 h). This precipitation scheme, which can be considered as a special case of the simplified Betts–Miller scheme (Wang et al.

Table 1 Parameters and their standard values used in the model

Parameter	Description	Typical value utilized here
C_0	Dry gravity wave speed of the baroclinic mode	50 m/s
ε	Rayleigh friction and Newtonian cooling coefficients	$(10\ day)^{-1}$ in dimensional unit
E	Nondimensional Ekman number in the boundary layer	0.68
τ	Convective adjustment time	12 h in dimensional unit
d	Nondimensional boundary layer depth	0.25
$\bar{Q}$	Normalized basic-state specific humidity stratifications of the middle atmosphere	0.81
$\bar{Q}_b$	Normalized basic-state specific humidity stratifications of the whole troposphere	1.79
SST	Sea surface temperature, which is used to determine $\bar{Q}$ and $\bar{Q}_b$	28.5 °C
L	Length Scale	1480 km
q_{ref}	Moisture Scale	32.65 kg/m^2
T_0	Time Scale	29,599 s
r	Radiation coefficient	0.2

More details can be found in Wang and Chen (2017)

2016), has been widely used in the MJO theoretical studies (Fuchs and Raymond 2005, 2017; Sobel and Maloney 2012, 2013; Adames and Kim 2016). Note that the system in this study is assumed to be a linear system and the precipitation is a small perturbation about a climatological background state.

2.2.2 Cloud radiation feedback

The cloud radiation anomaly is parameterized in such a way that the heating in the deep convection zone due to the reduction of the radiative cooling is proportional to convective heating (Fuchs and Raymond 2002, 2017; Peters and Bretherton 2005; Sobel and Maloney 2013; Adames and Kim 2016):

$$R = rPr \tag{9}$$

where r is the radiation coefficient, which is set to constant ($r = 0.2$) in this study.

2.3 Eigenvalue techniques

Equations (1–9) consist of a closed system. When wave solutions are assumed for all variables, the system becomes a linear eigenvalue system. Motivated by Gill (1980) and Majda and Stechmann (2009), we introduce the characteristic variables $q^c = u + \Phi$ and $r^c = -u + \Phi$. Supposing that $q^c = \sum_{n=0}^{\infty} q_n^c \varphi_n$, $r^c = \sum_{n=0}^{\infty} r_n^c \varphi_n$ and $q = \sum_{n=0}^{\infty} q_n \varphi_n$, where φ_n is the nth parabolic cylinder function, Eqs. (1–4) can be converted into characteristic equations (Gill 1980; Majda 2003).

Figure 3 shows the zeroth and second order parabolic cylinder functions, which are symmetric about the equator. The zeroth order parabolic cylinder function has a Gaussian bell shape with maximum at the equator, while the second order parabolic cylinder function has a triple-pole structure with minimum at the equator flanked by two maxima off the equator. As shown below, these two parabolic cylinder functions construct the Kelvin wave and the first symmetric equatorial Rossby wave.

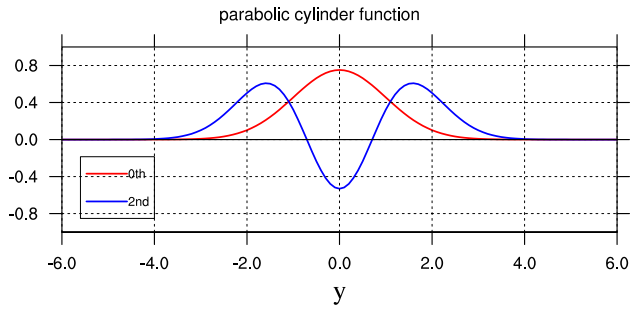

Fig. 3 Zeroth (red curve) and second (blue curve) order parabolic cylinder functions

If we assume that the forcing terms on the right-hand side of Eq. (3) and the moisture anomaly have a simple meridional structure proportional to $exp\left(-y^2/2\right)$ (zeroth order parabolic cylinder function), the characteristic equations can be reduced to a system that contains only the Kelvin wave and the first symmetric equatorial Rossby wave (Gill 1980; Majda and Stechmann 2009). Then, Eqs. (1–4) can be rewritten as:

$$\left(\frac{\partial}{\partial t} + \varepsilon\right)K + \frac{\partial K}{\partial x} = -F_0 \tag{10}$$

$$\left(\frac{\partial}{\partial t} + \varepsilon\right)R - \frac{1}{3}\frac{\partial R}{\partial x} = -\frac{\sqrt{2}}{3}F_0 \tag{11}$$

$$\frac{\partial q_0}{\partial t} + \bar{Q}\left(\frac{1}{2}\frac{\partial K}{\partial x} - \frac{1}{3\sqrt{2}}\frac{\partial R}{\partial x} - \frac{1}{6}F_0\right) + \bar{Q}_b dD_b^0 = -q_0/\tau \tag{12}$$

where $K = q_0^c$ denotes the Kelvin wave and $R = q_2^c$ denotes the Rossby wave. $F_0 = (1 + r)q_0/\tau + dD_b^0$, where $D_b^0 = \frac{1}{2}\left(K + \sqrt{2}R\right)e_{01} + \frac{R}{2}e_{02}$ is the projection of BL divergence to the zeroth order parabolic cylinder function. e_{01} and e_{02} are BL divergence coefficients. "Appendix" describes details about how to determine the BL divergence coefficients. The variables Φ, u and v can be recovered by using the following formulas:

$$\Phi = \frac{1}{2}\left(K + \sqrt{2}R\right)\varphi_0 + \frac{R}{2}\varphi_2 \tag{13}$$

$$u = \frac{1}{2}\left(K - \sqrt{2}R\right)\varphi_0 + \frac{R}{2}\varphi_2 \tag{14}$$

$$v = \left(\frac{2}{3}\frac{\partial R}{\partial x} - \frac{1}{3\sqrt{2}}F_0\right)\varphi_1 \tag{15}$$

Equations (10–12) provide a simple theoretical model for the MJO. The merit of this derivative model is that it consists of only the Kelvin wave and the first symmetric Rossby wave, and the total number of variables reduces to only three. This derivative model is capable of studying how propagation of the MJO mode is linked to the Kelvin and Rossby wave components. The model parameters are listed in Table 1. This derivative model is different from the one in Liu and Wang (2017), as in our study there is an assumption that moisture and precipitation have a simple meridional structure ($\sim e^{-y^2/2}$).

3 Basic features of the moisture mode

When the WF (stands for wave feedback) is turned off in the model (i.e. neglecting $\partial K/\partial t$ and $\partial R/\partial t$), the third order eigenvalue problem reduces to a first-order algebraic

equation if wave solutions are assumed. If the BL dynamics are further neglected (by setting d to zero), the model is essentially reduced to the "moisture mode" model (Sobel and Maloney 2013; Adames and Kim 2016). In this MM (stands for moisture mode) model, only two feedback processes are included: the MF (stands for moisture feedback) and CRF (stands for cloud radiation feedback).

To identify the respective roles of the MF and CRF, we first exclude the CRF (by setting r to zero) and regard the resulting mode as "pure" MM. As shown in Fig. 4, the phase speed of the pure MM decreases with increasing wavenumber (Fig. 4a). The phase speed is about 6 m/s at wavenumber one but nearly stationary for wavenumber 2–4 (0.5 ~ 2 m/s). The frequency of the pure MM (Fig. 4b) decreases with increasing wavenumber (or shorter waves have shorter periods) as well, which is inconsistent with observations (Fig. 1). The period for the pure MM is too long for wavenumber 2–4, which lies out of the intraseasonal range. The pure MM is a damping mode (Fig. 4c) with the longer waves being more damped.

In comparison with the pure MM, features of the MM with CRF are shown by the blue lines in Fig. 4a–c. The CRF has negligible effects on the eastward propagation speed and dispersion relation (Fig. 4a, b). It mainly acts to destabilize the MM (Fig. 4c). Although the growth rate rises as the CRF is included, the MM with CRF remains a damping mode when $\bar{Q} = 0.81$. However, if $\bar{Q}$ increases to a higher value of about 0.9 (corresponding to an SST value of about 30.5 °C), the MM becomes unstable (green line in Fig. 4c). It is worth noting that the CRF does not favor the planetary scale selection because the CRF-induced growth rate does not favor the longer wavelength.

4 Essential features of the dynamic moisture mode

When the WF, together with the BLCF (stands for boundary layer convergence feedback), is included, the linear system (Eqs. 10–12) constitutes a third-order eigenvalue problem. Solving this problem yields three modes. The first is a Kelvin-wave-like mode, with geopotential pattern and frequency resembling the Kelvin wave. The second is a Rossby-wave-like mode, with geopotential pattern and frequency resembling the Rossby wave. The third mode is a convectively coupled Kelvin–Rossby wave, with the Kelvin wave component located to the east of precipitation and the Rossby wave component to the west. This third mode is referred to as the DMM (stands for dynamic moisture mode). Comparing with the MM, two additional feedback processes are contained in the DMM, i.e., the BLCF and WF.

The dynamic features of the DMM are shown in Fig. 5 (red lines). The DMM exhibits an eastward propagation at wavenumber 1–4 and the propagation speed decreases with increasing wavenumber (Fig. 5a). This eastward propagating MJO-like mode has a period within the intraseasonal range (30–90 days, Fig. 5b). The DMM is an unstable mode with the growth rate rising with increasing wavelength, indicating a preferred planetary-scale unstable mode (Fig. 5c).

To identify the roles of the WF, we compare the DMM to the MM with BLCF (blue lines) in Fig. 5. The MM with BLCF has no WF but includes effects of the BLCF on the MM. There are several important differences between the MM with BLCF and the DMM, which highlight the impacts of the WF. First, contrasting to the MM with BLCF, the phase speed of the DMM at wavenumber 1–2 reduces dramatically (Fig. 5a): for wavenumber one, it is reduced from about 40 m/s to about 10 m/s; it is around 6 m/s at

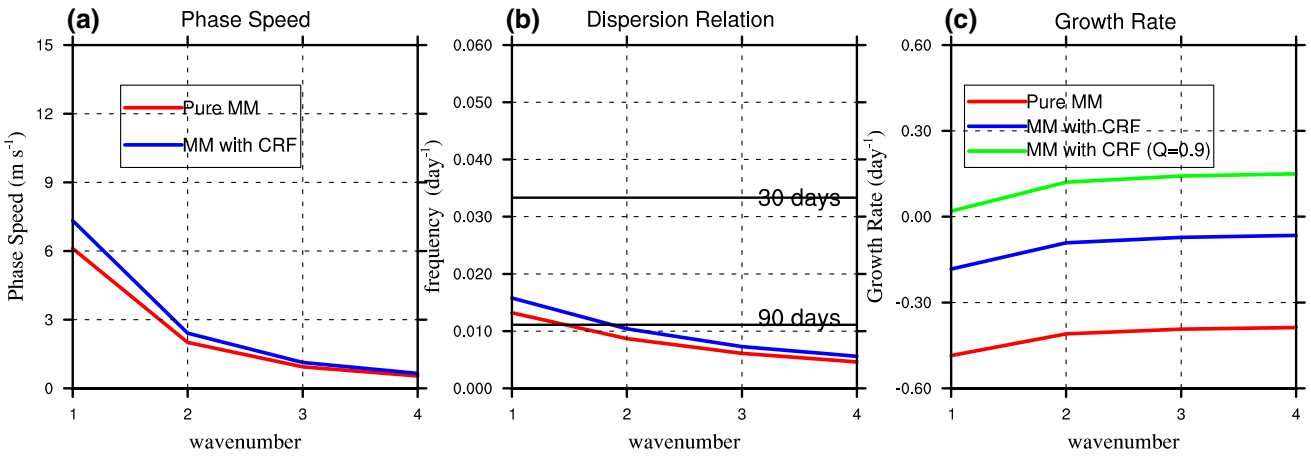

Fig. 4 Dynamic features of the moisture mode (MM): **a** phase speed, **b** dispersion relation and **c** growth rate. The red lines depict the pure MM and the blue lines depict the MM with CRF. In **c**, the MM with CRF under $\bar{Q} = 0.9$ is shown by the green line

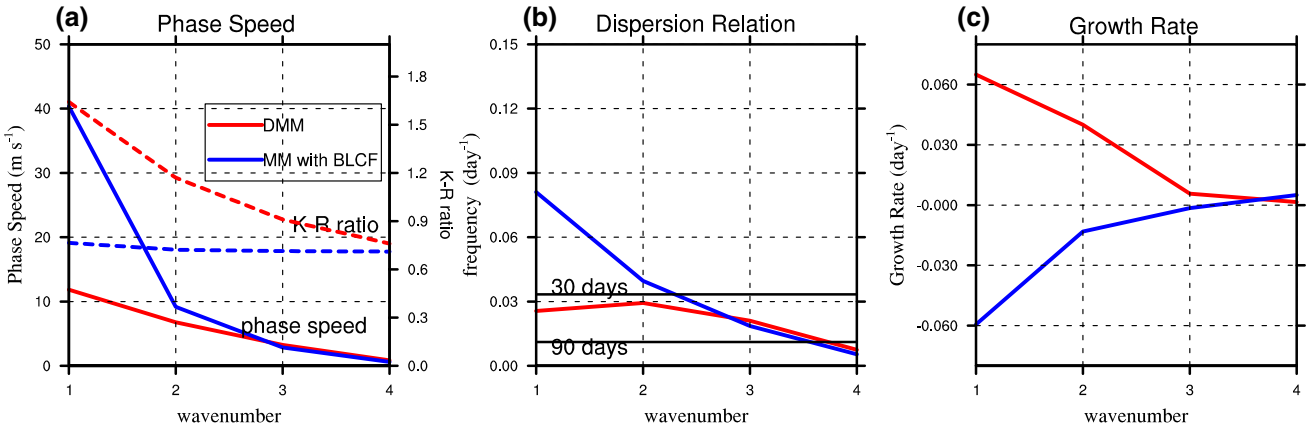

Fig. 5 Dynamic features of the dynamic moisture mode (DMM): **a** phase speed, **b** dispersion relation and **c** growth rate. The red lines depict the DMM and the blue lines depict the MM with BLCF. The dashed lines in **a** show the K–R ratios of the corresponding MJO modes

wavenumber two, which is close to observations. Second, the frequency of the DMM (red line, Fig. 5b) shows little variation at the planetary scales (wavenumber 1–3), which is close to observations (Fig. 1). Third, the DMM has a growth rate rising with increasing wavelength (Fig. 5c). In summary, it is the WF that selects wavenumber one as the most unstable mode and yields a more realistic dispersion relation.

To understand the aforementioned differences between the MM with BLCF and the DMM, we must examine their horizontal structures (Fig. 6). Note that the zonal winds are in strict geostrophic balance with the geopotential, as indicated by Eq. (2). Both the MM with BLCF and the DMM have coupled Kelvin–Rossby structures, with Kelvin wave to the east of precipitation and Rossby wave to the west. However, a prominent difference between them is seen for the long wave (wavenumber one). The DMM has a stronger Kelvin wave component than the MM, suggesting that the WF has significantly changed the structure of the most unstable planetary mode. Due to inclusion of the BLCF, BL convergence leads precipitation in both modes on wavenumber one. However, the phase leading of BL convergence to precipitation reduces on the shorter wavelength in both modes, as seen from Fig. 6.

The results of Fig. 6 suggest that the WF significantly changes the horizontal structures, which is manifested by the relative intensities between the Kelvin and Rossby waves. In the previous study of Wang and Chen (2017), the eastward phase propagation speed of the trio-interactive MJO mode is shown to be proportional to the relative intensity of the Kelvin versus Rossby wave component when the WF is included. For this reason, we define a K–R ratio to measure the relative intensity between the Kelvin and Rossby wave components. The K–R ratio here is defined as the ratio between the amplitudes of the Kelvin and Rossby wave components, i.e. $|K|/|R|$. The K–R ratios for the MM with BLCF and the DMM are shown in Fig. 5a by dashed lines. The MM with BLCF has a K–R ratio roughly independent of wavenumber; by contrast, the K–R ratio of the DMM decreases with increasing wavenumber and more importantly, its variation is correlated with that of the phase speed. This implies that the eastward propagation of the DMM is closely related to the relative intensity between the Kelvin and Rossby wave components, whereas in the MM, the propagation does not relate to the K–R ratio.

As the DMM involves the BLCF and CRF, it is interesting to explore the roles of the BLCF and CRF in shaping the dynamics of the DMM in the presence of the WF. Impacts of the BLCF on the DMM can be seen in the upper panels of Fig. 7 by turning on and off the BLCF. Evidently, the BLCF is the driver of the eastward propagation (Fig. 7a, b), because without the BLCF the propagation speed of the DMM drops below 1.5 m/s and the DMM becomes nearly stationary. In addition, the K–R ratio in the DMM decreases when the BLCF is turned off, indicating that the BLCF can accelerate the eastward propagation of the DMM by enhancing the relative intensity of the Kelvin wave component. Figure 7c shows that the BLCF not only destabilizes the DMM but also favor the planetary scale selection, because the increase of growth rate caused by the BLCF (DMM minus DMM without BLCF) is larger at the longer wavelengths.

The effects of the CRF on the DMM are shown in the lower panels of Fig. 7. The CRF can significantly slow down the eastward propagation speed of the DMM by about 3–4 m/s for wavenumber 1–4 (Fig. 7d), resulting in a more realistic oscillation period (Fig. 7e). This is realized through enhancing the relative intensity of the Rossby wave component (Fig. 7d). Figure 7f indicates that the CRF makes the DMM unstable, but it does not yield the planetary scale selection, as the increase of growth rate caused by the CRF (DMM minus DMM without CRF) is larger at the shorter wavelengths.

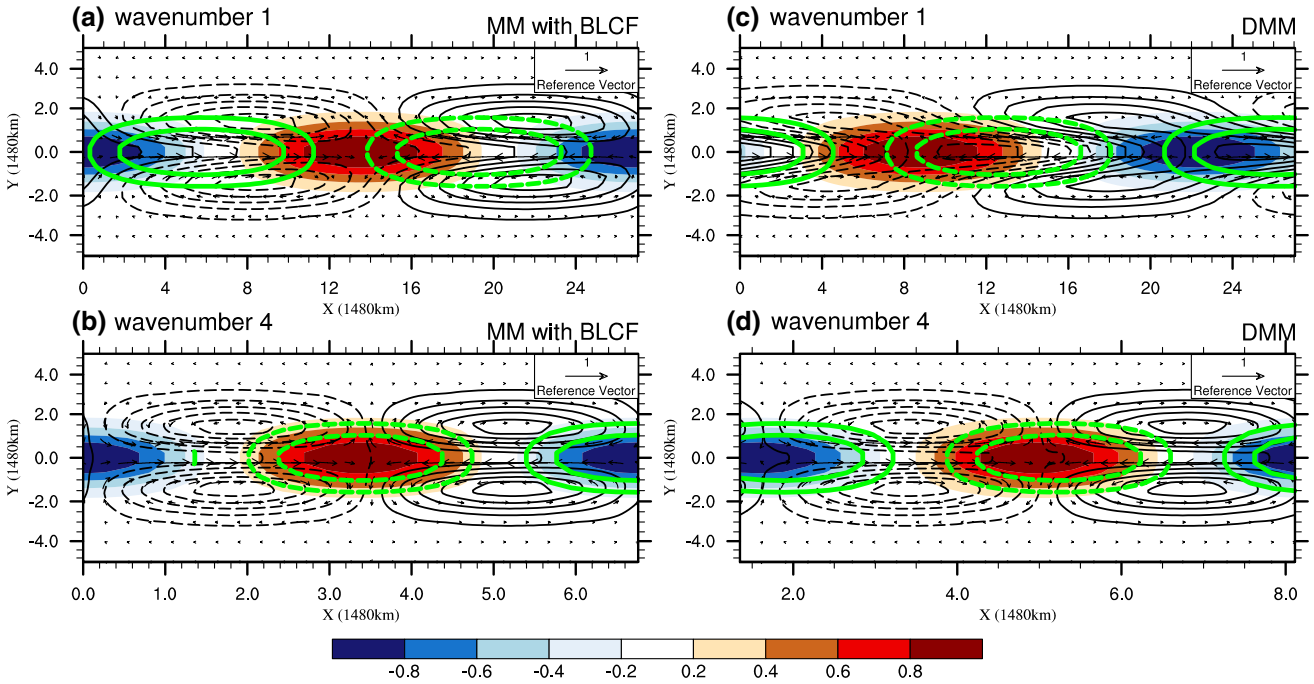

Fig. 6 Horizontal structures of the MM with BLCF (left panels) and the DMM (right panels) at wavenumber one (upper panels) and wavenumber four (lower panels). The black contour denotes low-level geopotential, the shading denotes precipitation, the vector denotes low-level wind, and the green contour denotes BL divergence, which is the projection to the lowest order parabolic cylinder function $\sim exp(-y^2/2)$. All fields have been normalized by their respective maximum (absolute value). The contour levels for BL divergence are ± 0.3 and ± 0.6. The black contour starts from -0.9 and has an interval of 0.2. In **a**–**d**, the maximum (absolute value) low-level wind speed, low-level geopotential, precipitation, and BL divergence, are 14.0/3.9/9.6/3.7 m/s, 272/72/161/67 m^2/s^2, 3/3/3/3 mm/day, and 9.5/1.5/9.6/1. 8×10^{-7}/s, respectively. Since the eigenvector has arbitrary amplitude, all variables are scaled to a 3 mm/day precipitation strength

Note that in Wang and Chen (2017), the BLCF alone can result in unstable mode, while in this study the additional CRF is needed. The difference is that in the present study, the basic state coefficient $\bar{Q}$ and $\bar{Q}_b$ are smaller than those used in Wang and Chen (2017), because the upper-level basic state moisture has been taken into account in this study (see "Appendix" for the details). Thus, in the present model, the BLCF alone cannot destabilize the MJO-mode for the given basic state SST at 28.5 °C. However, if we increase the values of $\bar{Q}$ and $\bar{Q}_b$ by increasing the SST (e.g. SST = 30.0 °C), the BLCF alone can destabilize the MJO-mode.

Table 2 further shows the relative magnitude of the *K, R* and *q* for the DMM (Fig. 5) and the MM (Fig. 4, with CRF). It shows that the relative magnitudes of each component in the DMM and MM show some consistency with the results of Majda and Stechmann (2009). Table 2 also shows the estimated relative magnitudes of the *K, R* and *q* in the observations (see "Appendix" for details about how to estimate them). Overall, the relative magnitudes of the *K, R* and *q* are comparable to those in the DMM. As shown in Table 2, the relative amplitudes of *K* and *R* (compared to *q*) in observation are smaller than those in the DMM. One possible reason for this is that the *q* may be overestimated (see "Appendix").

5 Different mechanisms behind fundamental dynamics between the MM and DMM

In Sects. 3 and 4, we have shown that the properties of the MM are quite different from those of the DMM. These differences are manifested in the eastward propagation speed, the wavenumber selection, the coupled horizontal structures and the dispersion relation (Figs. 4, 5, 6, 7). These differences are due to the dynamic feedbacks (WF and the BLCF). In this section, we explore how the dynamic feedbacks change these properties.

5.1 Mechanisms of eastward phase propagation

What drives the MM eastward? Since the only prognostic variable in the MM is moisture anomaly, the eastward propagation of the MM is determined solely by the eastward propagation of moisture anomaly, or equivalently, precipitation anomaly. The eastward propagation of the MM can be inferred from the moisture equation (Eq. 4) by neglecting BL convergence:

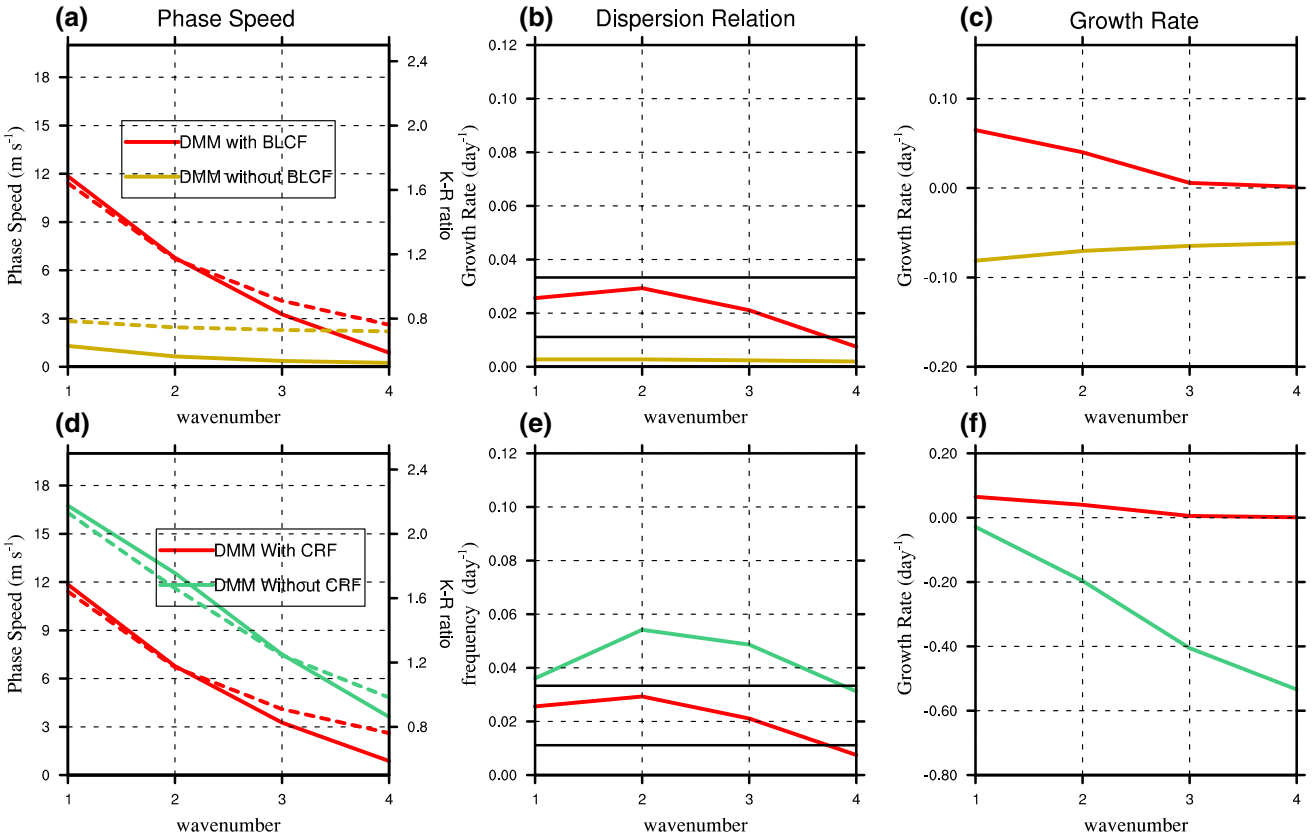

Fig. 7 Dynamic features of the DMM: phase speed (the first column), dispersion relation (the second column) and growth rate (the third column). The upper panels compare the DMM with the "DMM" excluding the BLCF; the lower panels compare the DMM with the "DMM" excluding the CRF. The dashed lines in **a, d** show the K–R ratios of the corresponding MJO modes

Table 2 Amplitudes of components of the eigenvector (*K, R* and *q*) in the DMM, MM and the observation

Components	DMM			MM		
	K	*R*	*q*	*K*	*R*	*q*
$k=1$	4.15	2.55	1.0	3.46	4.23	1.0
$k=2$	1.92	1.62	1.0	1.76	2.38	1.0
$k=3$	1.20	1.32	1.0	1.18	1.63	1.0
$k=4$	0.88	1.14	1.0	0.88	1.24	1.0
Observation	0.88	0.85	1.0			

For comparison, the amplitude of *q* is scaled to 1, and the amplitudes of *K* and *R* are scaled proportionally

$$\frac{\partial q}{\partial t} = -\bar{Q}\nabla\cdot\vec{V} - \frac{q}{\tau} \tag{16}$$

When damping is neglected ($\varepsilon = 0$), the convergence in Eq. (16) is balanced by the diabatic heating [$\nabla\cdot\vec{V} = -Pr - R$, from Eq. (3)]. Thus, Eq. (16) becomes:

$$\frac{\partial q}{\partial t} = \left[\bar{Q}(1+r) - 1\right]\frac{q}{\tau} \tag{17}$$

Without the CRF, the pure MM is a standing damping mode, because $\bar{Q} < 1$ for realistic SST (basic state moisture) values. When the CRF is included, the MM without damping is an unstable standing mode if $\bar{Q}(1+r) > 1$. With damping included, the free atmospheric convergence is no longer exactly in phase with diabatic heating:

$$\nabla\cdot\vec{V} = -(Pr - R) - \varepsilon\Phi \tag{18}$$

Physically, when there is no damping, the Kelvin wave and Rossby wave are in quadrature relation with the precipitation (e.g. $\frac{\partial K}{\partial x} = -Pr$). When damping is included, the Kelvin wave response would be shifted westward with respect to the precipitation (e.g. $\varepsilon K + \frac{\partial K}{\partial x} = -Pr$) while the Rossby wave response would be shifted eastward, which is also

shown by Adames and Kim (2016, their Fig. 1). The reason is that the free atmospheric friction (damping) reduces the eastward (westward) propagation of the forced Kelvin (Rossby) wave. Since the MM has stronger Rossby wave over Kelvin wave (as shown in Figs. 5a, 6), the eastward shift of the Rossby wave would lead to eastward shift of the low-level convergence. As shown in Fig. 8, the free atmospheric convergence leads (to the east of) precipitation due to the damping effect, and there is good correlation between this phase leading and the frequency for a fixed damping rate. Note that the free atmospheric convergence is large as it roughly balances the precipitation ($\frac{q}{\tau}$). Thus, a small phase leading of the free atmospheric convergence to the precipitation could result in a small but a significant nonzero eastward frequency.

Different from the MM, the circulation in the DMM is not a stationary response to convective heating. With the WF included, the heating-induced wave components (i.e. the Kelvin and Rossby waves) can propagate and the associated wave-induced moisture convergence (including both the free atmospheric and the BL moisture convergence) can feed back to the moisture field and affect convection. Thus, it is conceivable that the eastward propagation of the DMM is related to the propagation of the Kelvin and Rossby wave components.

This hypothesis is supported by the results in Figs. 5 and 7, which show that the phase propagation speed of the DMM is positively correlated with the K–R ratio. Note that although the Rossby wave have convergence located off the equator, the convection associated with the convectively Rossby wave are often near the equator in observations (Yang et al. 2007; Kiladis et al. 2009). Thus, the Rossby wave and Kelvin wave will have a combined convergence near the equator in phase with the convection when they are coupled together with the convection. An example for this is the Gill–Matsuno pattern (Matsuno 1966; Gill 1980). Since the Kelvin wave tends to propagate eastward while the Rossby wave tends to propagate westward, they have competing effects on the combined convergence and convection fields. Thus, a stronger Kelvin (Rossby) wave component will accelerate (retard) the eastward propagation of the DMM.

5.2 Planetary wave selection mechanism

It is shown that the growth rate in the MM rises with increasing wavenumber (Fig. 4c) while the opposite occurs in the DMM (Fig. 5c), indicating that the DMM has the planetary scale selection while the MM does not. What causes this difference?

For the MM, the amplification (decay) of the system is solely dependent on the amplification (decay) of the moisture perturbation, which relies mainly on whether the moisture supply contributed by the free atmospheric moisture convergence can overcome the moisture depletion resulted from precipitation (Eq. 16). Due to damping, the free atmospheric moisture convergence slightly leads precipitation. Since this phase leading decreases with increasing wavenumber (Fig. 8), less moisture convergence is supplied to overcome precipitation at longer wavelengths, resulting in a growth rate that increases with increasing wavenumber (Fig. 4c). When the CRF is included, it can promote the

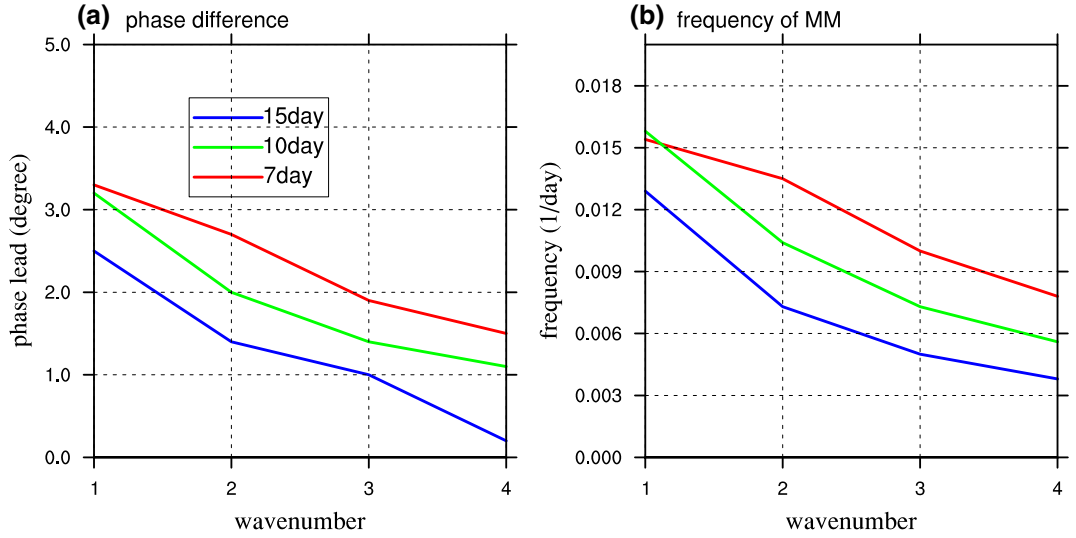

Fig. 8 Features of the free atmospheric convergence and frequency in the MM: **a** the phase leading of the free atmospheric convergence to the precipitation and **b** the associated dispersion relation. The blue, green and red curves correspond to damping time scales of 15 days, 10 days and 7 days

free atmospheric moisture convergence [as indicated by Eq. (17)], thereby raising the growth rate. For a constant radiation coefficient r, the increase of growth rate due to the CRF is roughly independent of wavenumber, as suggested by Eq. (17) and Fig. 4c. As a result, it explains why the MM doesn't have the planetary scale selection (Fig. 4c).

When the WF is included, the growth of the system is not solely dependent on the growth of moisture. To study the instability of the DMM, we investigate the perturbation column moist static energy (MSE) equation (see "Appendix" for derivation):

$$\frac{\partial}{\partial t}h = \left(1-\bar{Q}\right)\nabla\cdot\vec{V} - d\left(\bar{Q}_b - 1\right)\nabla\cdot\vec{V}_b + r\frac{q}{\tau} \tag{19}$$

where $h = q - \Phi$ is the perturbation MSE. Since the adiabatic cooling is larger than the latent heating induced by the low-level free atmospheric moisture convergence, $1-\bar{Q} > 0$, the first term on the right-hand side of Eq. (19) represents a damping of the perturbation MSE by the free atmospheric convergence. Since the latent heating resulting from the BL moisture convergence is larger than the damping effect of the BL, $\bar{Q}_b - 1 > 0$, the second term denotes intensification of the perturbation MSE by the BL convergence. The third term is the intensification of the perturbation MSE by the CRF.

Analogous to the available energy, we can define an eddy available MSE (EAMSE) in terms of $h^2/2$. This EAMSE is presumably related to the Lorenz's moist available energy (Lorenz 1978), as the perturbation MSE can be considered as a potential energy perturbation in the moist atmosphere. The equation of the EAMSE can be obtained by multiplying h to the both sides of the Eq. (19):

$$\frac{\partial}{\partial t}h^2/2 = \left(1-\bar{Q}\right)h\nabla\cdot\vec{V} - d\left(\bar{Q}_b - 1\right)h\nabla\cdot\vec{V}_b + rh\frac{q}{\tau} \tag{20}$$

The first term damps the EAMSE if positive h is in phase with the free atmospheric convergence. The second term increases the EAMSE if positive h is collocated with the BL convergence. Since the positive precipitation ($\frac{q}{\tau}$) is basically collocated with positive h, the CRF (third term) can enhance the EAMSE.

Why does the DMM mode have a preferred planetary scale? To address this question, we need to examine the phase relationship among perturbation MSE, low-level pressure, and BL moisture convergence for different wavelengths. Figure 9 shows the horizontal structures of the perturbation MSE for the DMM. On wavenumber 1, as the Kelvin wave low pressure is stronger (Fig. 9a), the maximum MSE is more collocated with the minimum low-level geopotential (Fig. 9a, b). On wavenumber 4, as the Kelvin wave low pressure is weaker,

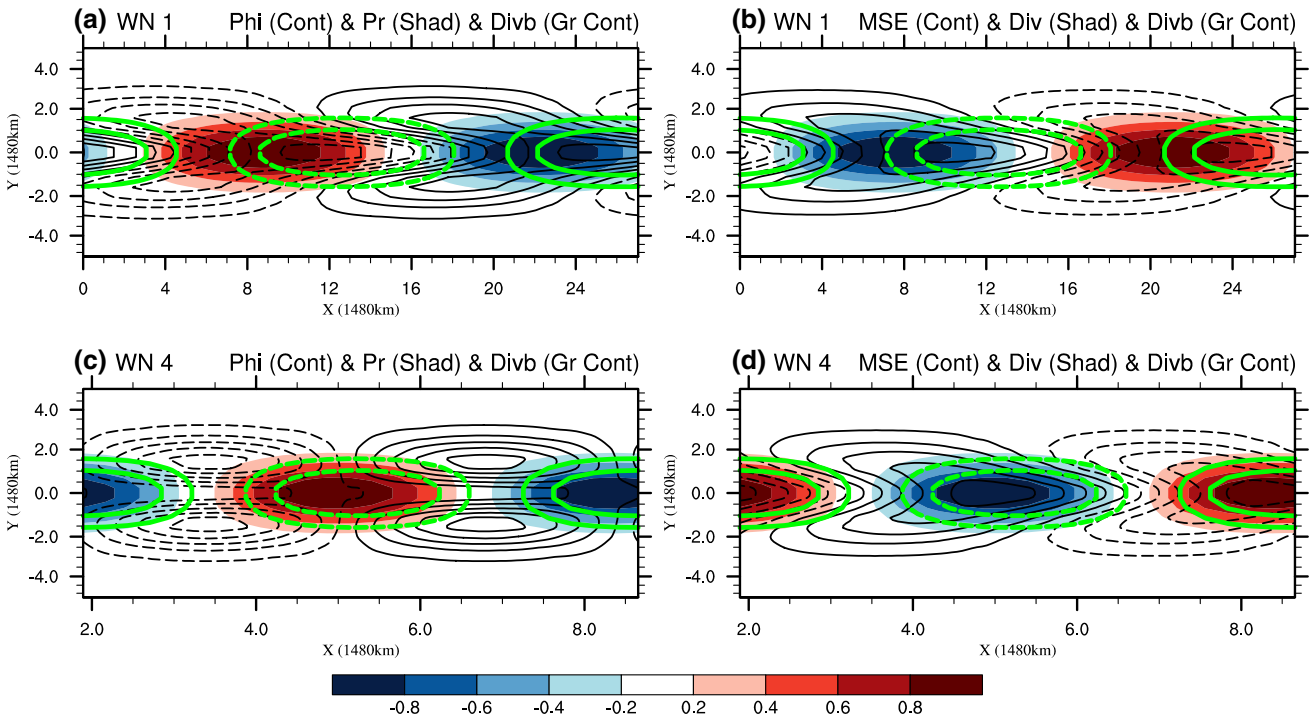

Fig. 9 The horizontal structures of the DMM for wavenumber 1 (upper) and wavenumber 4 (lower): (left) the geopotential (black contour), the precipitation (shading) and the boundary layer convergence (green contour); (right) the perturbation MSE (black contour), the low-level free atmospheric convergence (shading) and the boundary layer convergence (green contour). Positive (negative) values are denoted by the solid (dashed) contours. All fields have been normalized by their respective maximum (absolute value). The contour levels for BL divergence are ± 0.3 and ± 0.6. The black contour starts from -0.9 and has an interval of 0.2

the maximum MSE is more collocated with the precipitation (or equivalently the moisture, Fig. 9c, d). On both wavenumbers, the maximum perturbation MSE is collocated with the BL convergence (Fig. 9b, d). Thus, the BLCF is efficient in generating the EAMSE on both wavenumbers. On the other hand, the free atmospheric convergence is roughly in phase with the precipitation, especially for the wavenumber 4. Consequently, the free atmospheric convergence is located to the west of the maximum perturbation MSE on wavenumber 1, while it is largely collocated with the maximum perturbation MSE on wavenumber 4. Consequently, the damping of the EAMSE by the free atmospheric convergence is more efficient on shorter wavelengths. Given the comparable efficiency of BLCF-induced EAMSE generation, the difference in EAMSE damping efficiency explains why there is a planetary scale selection for the DMM.

The fundamental cause for this planetary scale selection is due to the phase difference between the BL convergence and the precipitation. For the longer waves the BL convergence precedes the precipitation by a larger phase leading, the BLCF-induced EAMSE generation tends to increase the Kelvin wave component, since it is in the Kelvin wave zone; as the Kelvin wave is intensified, the low-level Kelvin wave low-pressure will be enhanced, which tends to move the maximum perturbation MSE to the east of the precipitation such that the BLCF-induced EAMSE generation is more efficient while the damping of EAMSE by the free atmospheric convergence is less efficient. For the shorter waves, the smaller phase leading of the BL convergence to the precipitation is not favorable for enhancing the Kelvin wave. The reason why the BL convergence tends to have a larger phase leading to the precipitation on longer waves is explained in "Appendix".

5.3 Mechanisms responsible for the propagation–structure relationship

The present model only contains the Kelvin wave and the first symmetric equatorial Rossby wave, thus the difference in the horizontal structures can be, to some extent, quantified by the K–R ratio. As shown by Fig. 5a, the K–R ratio is roughly unchanged in the MM while it significantly decreases with increasing wavenumber in the DMM. How do the dynamic feedbacks cause this difference?

For the MM, the K–R ratio can be obtained through neglecting the time tendencies in Eqs. (10–11), substituting wave solutions into Eqs. (10–11), and then dividing Eq. (10) by Eq. (11):

$$\frac{|K|}{|R|} = \frac{3}{\sqrt{2}} \frac{|\varepsilon - ik/3|}{|\varepsilon + ik|} \tag{21}$$

Equation (21) shows that the K–R ratio in the MM is determined by the wavenumber and damping rate, thus it is not related to convective heating or the BLCF. For a small damping rate ($\varepsilon \approx 0$), it is shown that the K–R ratio for the MM is nearly a constant.

For the DMM, due to the WF, the BLCF-induced EAMSE generation enhances the Kelvin wave component, leading to a higher K–R ratio than that in the MM. The generation of EAMSE for the Kelvin wave is more efficient at longer wavelengths as explained in the Sect. 5.2, resulting in a K–R ratio decreasing with increasing wavenumber. By further examining Fig. 9, it shows that the generation of EAMSE by the CRF is more located in the Rossby wave zone, especially on the longer wavelengths, explaining why the CRF tends to reduce the K–R ratio (Fig. 7d).

5.4 Explanation of the dispersion relation

For the MM, its dispersion relation is determined by the moisture equation (Eq. 16), which can be written as:

$$-i\omega q = -\bar{Q}\left(\frac{\partial u}{\partial x} + \frac{\partial v}{\partial y}\right) - q/\tau \tag{22}$$

The right-hand side of the Eq. (22) represent the difference between moisture convergence and precipitation. For a larger phase leading of moisture convergence to the precipitation (or equivalently the moisture), there will be a larger frequency (real part of ω). Therefore, it explains the decreasing frequency with increasing wavenumber (Fig. 8).

With the dynamic feedbacks included, the frequency of the DMM is related to the Kelvin and Rossby wave components (Figs. 5, 7). Thus, it is conceivable that the dispersion relation of the DMM is affected by the dispersion relations of the Kelvin and Rossby wave components. Figure 10 shows the dispersion relations of the convectively coupled Kelvin and Rossby waves. The convectively coupled Kelvin (Rossby) wave is obtained by neglecting the Rossby (Kelvin) wave component in Eqs. (10–12). It should be noted that the convectively coupled Kelvin wave, the convectively coupled Rossby wave and the DMM are not three independent modes from the same equations. For example, the equations for the convectively coupled Kelvin wave are:

$$\left(\frac{\partial}{\partial t} + \varepsilon\right)K + \frac{\partial K}{\partial x} = -F_0 \tag{23}$$

$$\frac{\partial q_0}{\partial t} + \bar{Q}\left(\frac{1}{2}\frac{\partial K}{\partial x}\right) + \bar{Q}_b dD^0_{b(K\ only)} = -q_0/\tau \tag{24}$$

The modes of the convectively coupled Kelvin and Rossby wave are chosen as those having reasonable horizontal structures compared to observations.

It is shown (Fig. 10) that the frequency of the convectively coupled Kelvin (Rossby) wave increases ($\frac{\partial \omega}{\partial k} > 0$)

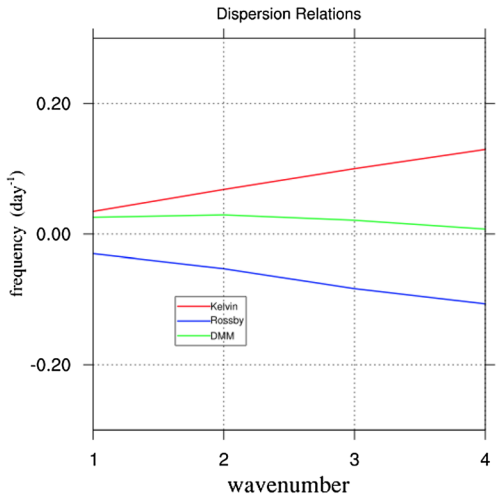

Fig. 10 Dispersion features of the DMM: the dispersion relations of the convectively coupled Kelvin wave (red), the convectively coupled Rossby wave (blue) and the DMM (green)

(decreases, $\frac{\partial \omega}{\partial k} < 0$) with increasing wavenumber. Since the DMM is a convectively coupled Kelvin–Rossby wave system, the increasing frequency contributed by the Kelvin wave component competes with the decreasing frequency caused by the Rossby wave component, thereby resulting in a frequency that is roughly independent of wavenumber ($\frac{\partial \omega}{\partial k} \approx 0$, Fig. 10, green curve, on wavenumber 1–3).

Note that since the K–R ratio decreases with increasing wavenumber, the frequency of the DMM leans towards the Rossby wave frequency more on the shorter wavelength (as shown in Fig. 10), and the frequency of the DMM is only a quasi-constant on the intraseasonal timescale. However, the frequency of the DMM is not a simple linear addition of the frequencies of convectively coupled Kelvin and Rossby waves.

6 Conclusion and discussion

6.1 Conclusion

In this study, the dynamical differences between the MM and the DMM are investigated by using theoretical MJO trio-interaction model. The MM of the MJO theory is governed by the MF (stands for moisture feedback) and CRF processes, whereas the DMM of the MJO theory includes additional WF and BLCF processes.

It is shown that the WF and the BLCF fundamentally change the properties of the MM. The MM has no planetary scale selection as the growth rate decreases with increasing wavelength. It has unrealistic low phase speed and low frequency at wavenumber 2–4. Meanwhile, the DMM has a planetary scale selection as the growth rate increases with increasing wavelength. The DMM has more realistic phase speed and dispersion relation at the planetary scales (wavenumber 1–3). Additionally, the horizontal structure (i.e. the K–R ratio) is roughly fixed and independent of the propagation speed in the MM, whereas in the DMM the propagation speed is related to the horizontal structure. These fundamental differences between the two MJO modes lie in the WF and the BLCF.

The WF and BLCF provide a mechanism for selecting planetary scale instability. Without the WF, the amplification of the MM depends on amplification of moisture or precipitation anomaly. The CRF can destabilize the MM by increasing the free atmospheric moisture convergence, but it does not have the planetary scale selection. With the WF, the amplification of the DMM depends on the generation of EAMSE (stands for eddy available MSE) by the BLCF. Due to the properties of the BL convergence, the generation of EAMSE is more efficient at longer wavelengths, resulting in planetary wave selection. This result extended the conclusion obtained for a convectively coupled kelvin waves (Wang 1988).

The WF and BLCF modify the horizontal structure of the MJO. The horizontal structures of the MM and the DMM can be measured by the ratio of the relative intensity between the Kelvin and Rossby wave components (i.e. the K–R ratio). In the MM, the K–R ratio is relatively small and roughly independent of wavenumber. With the WF and the BLCF, the Kelvin wave in the DMM is significantly stronger than that in the MM at longer wavelengths due to the BLCF-induced EAMSE, leading to a higher K–R ratio at longer wavelengths.

The WF and BLCF affect the MJO propagation. Without the WF and BLCF, the eastward propagation of the MM is driven by the small phase leading of the free atmospheric convergence to the precipitation, resulting in a very slow eastward propagation. With the WF, the eastward propagation of the DMM is driven by the Kelvin wave component, and its phase speed is correlated with the K–R ratio. A stronger Kelvin (Rossby) wave component promotes (retards) the eastward propagation. Moreover, the BLCF accelerates the eastward propagation of the DMM by enhancing the Kelvin wave component, while the CRF retards the eastward propagation by strengthening the Rossby wave component. Without the BLCF, the DMM becomes a quasi-standing mode, indicating the importance of the BLCF.

The WF and BLCF are important for explaining the observed dispersion relationship of the MJO. Without the WF and the BLCF, the dispersion relation of the MM is primarily controlled by the phase difference between the free atmospheric moisture convergence and precipitation, which results in unrealistic periodicity and dispersion relation.

With the WF, the dispersion relation of the DMM is related to the Kelvin and Rossby wave components. Since the Kelvin-wave (Rossby-wave) frequency increases (decreases) with increasing wavenumber, the coupling of the Kelvin and Rossby wave components in the DMM yields a balanced quasi-constant frequency at the planetary scales (wavenumber 1–3). The BLCF increases the frequency to a reasonable value by enhancing the Kelvin wave component.

6.2 Discussion

Since the presence of the dynamic feedbacks (WF and the BLCF) can substantially change properties of the MJO mode, cautions should be exercised when interpreting the results obtained from the models without the dynamic feedbacks. It is more advisable to retain the WF and the BLCF in the theoretical study of the MJO. Additionally, the results of this study suggest that the moisture mode theory can be considerably improved by adding the WF and the BLCF.

The results of this study also suggest that in order to obtain better MJO simulations, the present-day GCM should improve its ability in simulating the interaction between the wave dynamics and the convection. As shown in Sect. 5, the WF and the BLCF tend to enhance the Kelvin wave on the planetary scale. In fact, by studying 24 model outputs that participated MJOTF/GASS Global Model Evaluation Project, Wang and Lee (2017) found that the good GCMs that can simulate the eastward propagation of the MJO tend to have higher K–R ratio than the poor GCMs that only simulate the nonpropagating MJO. Moreover, the leading BL convergence is well simulated in the good GCMs but is missing in the poor GCMs. These imply that the effects of the WF and BLCF are poorly represented in some GCMs, which impedes model's ability in simulating the MJO.

The finding that the eastward propagation of the MJO-mode is related to the Kelvin and Rossby waves in the presence of the WF is supported by results obtained from the diagnostic study of the multi-GCM results by Wang and Lee (2017), and the GCM study by Kang et al. (2013), which showed that the MJO propagates faster (slower) when the Kelvin (Rossby) wave component is enhanced. Pritchard and Yang (2016) also revealed that propagation of the MJO-mode in the GCM is related to the equatorial waves, especially the Kelvin wave. However, it is unclear whether the propagation speed of the observed MJO has the same relation with the Kelvin and Rossby wave components. Further study is under way to verify this relation through observations.

Acknowledgements This work is jointly supported by the National Natural Science Foundation of China (Grant no. 41420104002) and the National Key Research and Development Program of China (Grant no. 2016YFA0600401), the NSF/Climate Dynamics Award #AGS-1540783, NOAA/CVP Award #NA15OAR4310177, the Public Science and Technology Research Funds Project of Ocean (201505013) and the Atmosphere-Ocean Research Center sponsored by the Nanjing University of Information Science and Technology and University of Hawaii. This is the SEOST publication 10453, IPRC publication 1342 and ESMC publication 235.

Open Access This article is distributed under the terms of the Creative Commons Attribution 4.0 International License (http://creativecommons.org/licenses/by/4.0/), which permits unrestricted use, distribution, and reproduction in any medium, provided you give appropriate credit to the original author(s) and the source, provide a link to the Creative Commons license, and indicate if changes were made.

Appendix

The moisture equation

As shown in Wang and Chen (2017), the dimensional moisture equation in the trio-interaction model can be expressed as [Eq. (29) in their paper]:

$$\frac{\partial q^*}{\partial t} + \frac{1}{g}\left[\omega_2\left(\bar{Q}_3^* - \bar{Q}_1^*\right) + \omega_e\left(\bar{Q}_e^* - \bar{Q}_3^*\right)\right] = -Pr^* \tag{25}$$

where $\omega_2^* = \Delta p\left(\frac{\partial u^*}{\partial x} + \frac{\partial v^*}{\partial y}\right) + \omega_e^*$ is the vertical velocity at the middle of the free atmosphere and $\omega_e^* = d\Delta p\left(\frac{\partial u_b^*}{\partial x} + \frac{\partial v_b^*}{\partial y}\right)$ is the vertical velocity at the top of the BL. The asterisk denotes that the variable is dimensional. $\bar{Q}_1^*$, $\bar{Q}_3^*$ and $\bar{Q}_e^*$ are the dimensional basic state specific humidity at the upper layer, the lower layer and the BL, which are controlled by the underlying SST. Substituting ω_2^* and ω_e^* into Eq. (25), we have:

$$\begin{aligned}\frac{\partial q^*}{\partial t} + \frac{\Delta p}{g}\Bigg[&\left(\frac{\partial u^*}{\partial x} + \frac{\partial v^*}{\partial y}\right)\left(\bar{Q}_3^* - \bar{Q}_1^*\right)\\ &+d\left(\frac{\partial u_b^*}{\partial x} + \frac{\partial v_b^*}{\partial y}\right)\left(\bar{Q}_e^* - \bar{Q}_1^*\right)\Bigg] = -Pr^*\end{aligned} \tag{26}$$

If we nondimensionalize Eq. (26) using the dimensional scales in Sect. 2.1, we have:

$$\frac{\partial q}{\partial t} + \bar{Q}\left(\frac{\partial u}{\partial x} + \frac{\partial v}{\partial y}\right) + d\bar{Q}_b\left(\frac{\partial u_b}{\partial x} + \frac{\partial v_b}{\partial y}\right) = -Pr \tag{27}$$

where $\bar{Q} = \left(\bar{Q}_3 - \bar{Q}_1\right)$ and $\bar{Q}_b = \left(\bar{Q}_e - \bar{Q}_1\right)$. The difference between the present study and Wang and Chen (2017) is that the $\bar{Q}_1$ is included in the present study.

The boundary layer divergence

As shown by Eq. (5), the BL divergence can be expressed in terms of the low-level geopotential. The geopotential in the eigenvalue system can be expressed in terms of the Kelvin and Rossby wave components (Eq. 13). Substituting Eq. (13)

into Eq. (7) and projecting the results onto the lowest order parabolic cylinder function, we have:

$$D_b^0 = \frac{1}{2}\left(K + \sqrt{2}R\right)e_{01} + \frac{R}{2}e_{02} \tag{28}$$

where D_b^0 is the projection of the BL divergence onto the zeroth order parabolic cylinder function. Coefficients e_{01} and e_{02} are:

$$\begin{aligned} e_{01} = &-k^2\int_{-\infty}^{\infty}\frac{-E}{E^2+y^2}\varphi_0^2 dy + \int_{-\infty}^{\infty}\frac{E\left(1-y^2\right)}{E^2+y^2}\varphi_0^2 dy \\ &+ ik\int_{-\infty}^{\infty}\frac{E^2-y^2}{\left(E^2+y^2\right)^2}\varphi_0^2 dy \\ &+ \int_{-\infty}^{\infty}\frac{2E}{\left(E^2+y^2\right)^2}\left(-\frac{1}{2}\varphi_0 - \frac{1}{\sqrt{2}}\varphi_2\right)\varphi_0 dy \end{aligned} \tag{29}$$

$$\begin{aligned} e_{02} = &-k^2\int_{-\infty}^{\infty}\frac{-E}{E^2+y^2}\varphi_0\varphi_2 dy + \int_{-\infty}^{\infty}\frac{E\left(5-y^2\right)}{E^2+y^2}\varphi_0\varphi_2 dy \\ &+ ik\int_{-\infty}^{\infty}\frac{E^2-y^2}{\left(E^2+y^2\right)^2}\varphi_0\varphi_2 dy \\ &+ \int_{-\infty}^{\infty}\frac{2E}{\left(E^2+y^2\right)^2}\left(\frac{\sqrt{2}}{2}\varphi_0 - \frac{1}{2}\varphi_2 - \sqrt{3}\varphi_4\right)\varphi_0 dy \end{aligned} \tag{30}$$

where k is the nondimensional wavenumber. φ_0, φ_2 and φ_4 are the zeroth, second and fourth order parabolic cylinder functions.

The moist static energy equation

The vertically integrated MSE is defined as $\frac{1}{g}\int_{P_0}^{P_s}(C_pT + \Phi + L_cq)dp$ in dimensional form. The nondimensional vertically integrated moisture in the current model is q. Since the temperature is proportional to the thickness of the atmosphere (i.e. the baroclinic part of the geopotential, see Wang and Chen 2017), it can be shown that the nondimensional vertically integrated enthalpy (C_pT) in the current model can be expressed as $-\Phi$. Since the model contains only the first baroclinic motion, the vertical integration of the potential energy (geopotential) in free atmosphere is zero, while the potential energy contributed from the BL is two orders of magnitude smaller than the enthalpy and is thereby neglected. Therefore, the nondimensional perturbation column MSE in the current model is $h = q - \Phi$. The perturbation MSE equation can be derived by subtracting Eq. (3) from Eq. (4):

$$\frac{\partial}{\partial t}h = \left(1-\bar{Q}\right)\nabla\cdot\vec{V} - d\left(\bar{Q}_b - 1\right)\nabla\cdot\vec{V}_b + r\frac{q}{\tau} \tag{31}$$

The phase difference between the BL convergence and precipitation

As shown in Sect. 5, the combined effect of the WF and the BLCF favors enhancement of the Kelvin wave at longer scales. This selection of planetary scale Kelvin wave is caused by the decreasing phase leading of BL convergence to precipitation, which decreases with increasing wavenumber. One reason for this is that for the same horizontal structure, the phase leading of BL convergence to precipitation tends to decrease with increasing wavenumber, which can be explained as follows.

Let us consider the expression of BL divergence (Eq. 7). The second term on the right-hand side of Eq. (7) is proportional to $\sim \frac{\partial\Phi}{\partial x}$. This term is in quadrature with the low-level low pressure for wave solutions and lags the low pressure by 1/4 wavelength. Since this term grows as the wavenumber increases ($\frac{\partial\Phi}{\partial x} \sim ik\Phi$), it can potentially shift the

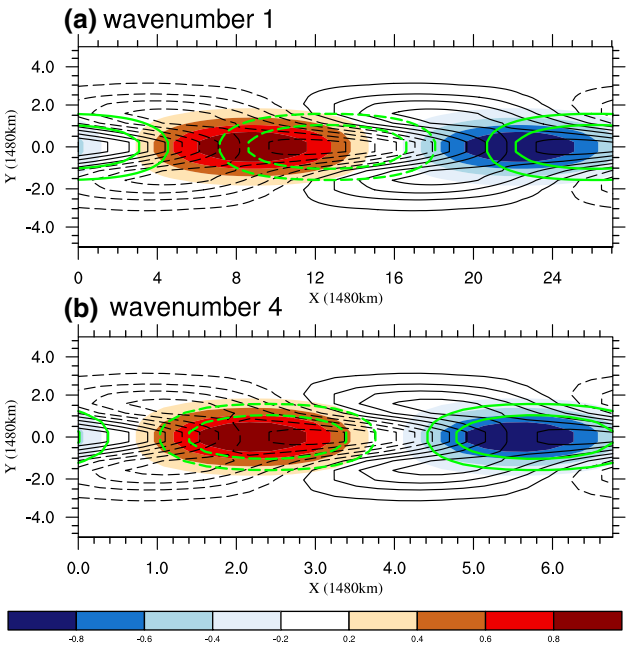

Fig. 11 Dependence of phase difference between BL convergence and precipitation on the zonal scale: horizontal structures on **a** wavenumber one and **b** wavenumber four. Circulation patterns in **a** and **b** are identical except for different wavelengths. The black contour denotes the geopotential, the shading denotes the precipitation, and the green contour denotes the BL divergence. All fields have been normalized by their respective maximum (absolute value). The contour levels for BL divergence are ±0.3 and ±0.6. The black contour starts from −0.9 and has an interval of 0.2

BL convergence westward. Thus, this term can contribute to the westward shift of the BLCF with respect to the low-level low-pressure center as the wavenumber increases. To illustrate this, Fig. 11 shows the horizontal circulation patterns and the associated BL divergence for wavenumber one and four. The horizontal patterns in Fig. 11a, b are identical except for different zonal wavelengths. Comparing Fig. 11a, b, one can find that for the same horizontal structure, the phase leading of BL convergence to precipitation decreases as wavenumber increases.

Estimation of *K, R* and *q* from observations

The datasets used are the daily ERA-Interim reanalysis dataset (Dee et al. 2011) for the 34 boreal winter seasons (November to April) from 1979 to 2013, and the daily NCEP/NOAA interpolated OLR dataset (Liebmann and Smith 1996). The *K, R* and *q* from the observations can be estimated by the following steps: (1) define $q_c = u + g \times z/C$, where C = 50 m/s is the speed of gravity wave, and define column integrated moisture q as vertically integrated specific humidity from 1000 to 200 hPa; define $q_c^{baroclinic} = (q_c^{700\text{hPa}} - q_c^{200\text{hPa}})/2$. (2) Filter the $q_c^{baroclinic}$ and q by removing seasonal cycle and applying a 20–70-day bandpass filter. (3) Define an OLR index by averaging filtered (same filtering in step 2) OLR over [10°S–10°N, 80°E–100°E]. (4) Regress the column q and $q_c^{baroclinic}$ against the OLR index and filter out the higher wavenumber to only retain zonal wavenumber 1–4. (5) Nondimensionalize the regressed column q and $q_c^{baroclinic}$ by using same dimensional scales as in the DMM. Figure 12 shows the nondimensional column q and $q_c^{baroclinic}$ along the equator (5°S–5°N). The K can be estimated as the absolute value of the minimum $q_c^{baroclinic}$, the R the maximum $q_c^{baroclinic}$ and the q the maximum column q. This estimation of R is better than projecting q_c onto the second parabolic cylinder function as suggested by the theoretical definition of R (Sect. 2.3), because the projection will be contaminated by the influences of subtropical jet stream and perturbations that come from midlatitudes. The estimated *K, R* and *q* are listed in Table 2. Since the moisture is more concentrated in the equatorial region, the q will be smaller when it is projected to the zeroth parabolic cylinder function (an assumption made about q and Pr), comparing to the current estimation (5°S–5°N averaging). Thus, the q may be overestimated in the Fig. 12.

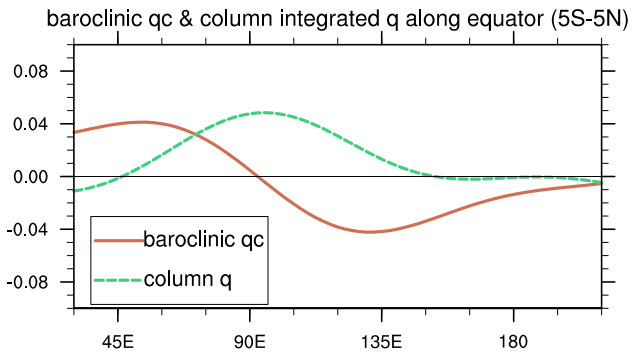

Fig. 12 Nondimensional observed baroclinic q_c and column integrated q along the equator (5°S–5°N). Only the wavenumber 1–4 are retained

References

Adames ÁF, Kim D (2016) The MJO as a dispersive, convectively coupled moisture wave: theory and observations. J Atmos Sci. https://doi.org/10.1175/JAS-D-15-0170.1

Adames ÁF, Wallace JM (2014) Three-dimensional structure and evolution of the vertical velocity and divergence fields in the MJO. J Atmos Sci 71:4661–4681. https://doi.org/10.1175/JAS-D-14-0091.1

Andersen JA, Kuang Z (2012) Moist static energy budget of MJO-like disturbances in the atmosphere of a zonally symmetric aquaplanet. J Clim 25:2782–2804. https://doi.org/10.1175/JCLI-D-11-00168.1

Arnold NP, Kuang Z, Tziperman E (2013) Enhanced MJO-like variability at high SST. J Clim 26:988–1001. https://doi.org/10.1175/jcli-d-12-00272.1

Benedict JJ, Randall DA (2007) Observed characteristics of the MJO relative to maximum rainfall. J Atmos Sci 64:2332–2354

Bony S, Emanuel KA (2005) On the role of moist processes in tropical intraseasonal variability: cloud–radiation and moisture–convection feedbacks. J Atmos Sci 62:2770–2789. https://doi.org/10.1175/JAS3506.1

Bretherton CS, Peters ME, Back LE (2004) Relationships between water vapor path and precipitation over the tropical oceans. J Clim 17:1517–1528

Chen G, Wang B (2017) Reexamination of the wave activity envelope convective scheme in theoretical modeling of MJO. J Clim 30:1127–1138. https://doi.org/10.1175/jcli-d-16-0325.1

Chen G, Wang B (2018) Does the MJO have a westward group velocity? J Clim 31:2435–2443. https://doi.org/10.1175/jcli-d-17-0446.1

Crueger T, Stevens B (2015) The effect of atmospheric radiative heating by clouds on the Madden–Julian Oscillation. J Adv Model Earth Syst 7:854–864. https://doi.org/10.1002/2015MS000434

Dee D et al (2011) The ERA-Interim reanalysis: Configuration and performance of the data assimilation system. Q J R Meteorol Soc 137:553–597

Emanuel KA (1987) An air–sea interaction model of intraseasonal oscillations in the tropics. J Atmos Sci 44:2324–2340 https://doi.org/10.1175/1520-0469(1987)044%3C2324:AASIMO%3E2.0.CO;2

Feng J, Li T, Zhu W (2015) Propagating and nonpropagating MJO events over Maritime Continent. J Clim 28:8430–8449

Fuchs Ž, Raymond DJ (2002) Large-scale modes of a nonrotating atmosphere with water vapor and cloud–radiation feedbacks. J Atmos Sci 59:1669–1679 https://doi.org/10.1175/1520-0469(2002)059%3C1669:LSMOAN%3E2.0.CO;2

Fuchs Ž, Raymond DJ (2005) Large-scale modes in a rotating atmosphere with radiative-convective instability and WISHE. J Atmos Sci 62:4084–4094

Fuchs Ž, Raymond DJ (2017) A simple model of intraseasonal oscillations. J Adv Model Earth Syst 9:1195–1211. https://doi.org/10.1002/2017MS000963

Gill AE (1980) Some simple solutions for heat-induced tropical circulation. Q J R Meteorol Soc 106:447–462

Hendon HH, Salby ML (1994) The life cycle of the Madden–Julian oscillation. J Atmos Sci 51:2225–2237 https://doi.org/10.1175/1520-0469(1994)051%3C2225:TLCOTM%3E2.0.CO;2

Hendon HH, Wheeler MC (2008) Some space–time spectral analyses of tropical convection and planetary-scale waves. J Atmos Sci 65:2936–2948. https://doi.org/10.1175/2008jas2675.1

Hsu P-c, Li T (2012) Role of the boundary layer moisture asymmetry in causing the eastward propagation of the Madden–Julian oscillation*. J Clim 25:4914–4931. https://doi.org/10.1175/JCLI-D-11-00310.1

Huffman GJ et al (2007) The TRMM multisatellite precipitation analysis (TMPA): quasi-global, multiyear, combined-sensor precipitation estimates at fine scales. J Hydrometeorol 8:38–55 doi. https://doi.org/10.1175/JHM560.1

Johnson RH, Ciesielski PE Jr, Katsumata JHR M (2015) Sounding-based thermodynamic budgets for DYNAMO. J Atmos Sci 72:598–622. https://doi.org/10.1175/jas-d-14-0202.1

Kang I-S, Liu F, Ahn M-S, Yang Y-M, Wang B (2013) The role of SST structure in convectively coupled Kelvin–Rossby waves and its implications for MJO formation. J Clim 26:5915–5930

Kiladis GN, Wheeler MC, Haertel PT, Straub KH, Roundy PE (2009) Convectively coupled equatorial waves. Rev Geophys 47:2

Knutson TR, Weickmann KM, Kutzbach JE (1986) Global-scale intraseasonal oscillations of outgoing longwave radiation and 250 mb zonal wind during northern hemisphere summer. Mon Weather Rev 114:605–623 https://doi.org/10.1175/1520-0493(1986)114%3C0605:GSIOOO%3E2.0.CO;2

Lau KM, Peng L (1987) Origin of low-frequency (intraseasonal) oscillations in the tropical atmosphere. Part I: Basic theory. J Atmos Sci 44:950–972 https://doi.org/10.1175/1520-0469(1987)044%3C0950:OOLFOI%3E2.0.CO;2

Liebmann B, Smith C (1996) Description of a complete (interpolated) outgoing longwave radiation dataset. Bull Am Meteorol Soc 77:1275–1277

Liu F, Wang B (2012) A frictional skeleton model for the Madden–Julian oscillation*. J Atmos Sci 69:2749–2758. https://doi.org/10.1175/JAS-D-12-020.1

Liu F, Wang B (2016) Effects of moisture feedback in a frictional coupled Kelvin–Rossby wave model and implication in the Madden–Julian oscillation dynamics. Clim Dyn:1–10

Liu F, Wang B (2017) Roles of the moisture and wave feedbacks in shaping the Madden–Julian oscillation. J Clim. https://doi.org/10.1175/jcli-d-17-0003.1

Lorenz EN (1978) Available energy and the maintenance of a moist circulation. Tellus 30:15–31. https://doi.org/10.1111/j.2153-3490.1978.tb00815.x

Madden RA, Julian PR (1971) Detection of a 40–50 day oscillation in the zonal wind in the Tropical Pacific. J Atmos Sci 28:702–708 https://doi.org/10.1175/1520-0469(1971)028%3C0702:DOADOI%3E2.0.CO;2

Madden RA, Julian PR (1972) Description of global-scale circulation cells in the tropics with a 40–50 day period. J Atmos Sci 29:1109–1123 https://doi.org/10.1175/1520-0469(1972)029%3C1109:DOGSCC%3E2.0.CO;2

Majda A (2003) Introduction to PDEs and waves for the atmosphere and ocean, vol 9. American Mathematical Society, Providence

Majda AJ, Stechmann SN (2009) The skeleton of tropical intraseasonal oscillations. Proc Natl Acad Sci 106:8417–8422

Maloney ED, Hartmann DL (1998) Frictional moisture convergence in a composite life cycle of the Madden–Julian oscillation. J Clim 11:2387–2403 https://doi.org/10.1175/1520-0442(1998)011%3C2387:FMCIAC%3E2.0.CO;2

Matsuno T (1966) Quasi-geostrophic motions in the equatorial area. J Meteorol Soc Jpn 44:25–43

Matthews AJ (2000) Propagation mechanisms for the Madden–Julian oscillation. Q J R Meteorol Soc 126:2637–2651

Neelin JD, Held IM, Cook KH (1987) Evaporation-wind feedback and low-frequency variability in the tropical atmosphere. J Atmos Sci 44:2341–2348 https://doi.org/10.1175/1520-0469(1987)044%3C2341:EWFALF%3E2.0.CO;2

Ogrosky HR, Stechmann SN (2015) Assessing the equatorial long-wave approximation: asymptotics and observational data analysis. J Atmos Sci 72:4821–4843 doi. https://doi.org/10.1175/JAS-D-15-0065.1

Peters ME, Bretherton CS (2005) A simplified model of the Walker circulation with an interactive ocean mixed layer and cloud-radiative feedbacks. J Clim 18:4216–4234 doi. https://doi.org/10.1175/JCLI3534.1

Pritchard MS, Yang D (2016) Response of the superparameterized Madden–Julian oscillation to extreme climate and basic-state variation challenges a moisture mode view. J Clim 29:4995–5008 doi. https://doi.org/10.1175/JCLI-D-15-0790.1

Raymond DJ (2001) A new model of the Madden–Julian oscillation. J Atmos Sci 58:2807–2819 https://doi.org/10.1175/1520-0469(2001)058%3C2807:ANMOTM%3E2.0.CO;2

Sobel A, Maloney E (2012) An idealized semi-empirical framework for modeling the Madden–Julian oscillation. J Atmos Sci 69:1691–1705

Sobel A, Maloney E (2013) Moisture modes and the eastward propagation of the MJO. J Atmos Sci 70:187–192. https://doi.org/10.1175/JAS-D-12-0189.1

Wang B (1988) Dynamics of tropical low-frequency waves: an analysis of the moist Kelvin wave. J Atmos Sci 45:2051–2065 https://doi.org/10.1175/1520-0469(1988)045%3C2051:DOTLFW%3E2.0.CO;2

Wang B, Chen G (2017) A general theoretical framework for understanding essential dynamics of Madden–Julian oscillation. Clim Dyn 49:2309–2328. https://doi.org/10.1007/s00382-016-3448-1

Wang B, Lee S-S (2017) MJO propagation shaped by zonal asymmetric structures: results from 24 GCM simulations. J Clim 30:7933–7952. https://doi.org/10.1175/jcli-d-16-0873.1

Wang B, Li T (1994) Convective interaction with boundary-layer dynamics in the development of a tropical intraseasonal system. J Atmos Sci 51:1386–1400 https://doi.org/10.1175/1520-0469(1994)051%3C1386:CIWBLD%3E2.0.CO;2

Wang B, Rui H (1990a) Dynamics of the coupled moist Kelvin–Rossby wave on an equatorial β-plane. J Atmos Sci 47:397–413 https://doi.org/10.1175/1520-0469(1990)047%3C0397:DOTCMK%3E2.0.CO;2

Wang B, Rui H (1990b) Synoptic climatology of transient tropical intraseasonal convection anomalies: 1975–1985. Meteorol Atmos Phys 44:43–61

Wang B, Liu F, Chen G (2016) A trio-interaction theory for Madden–Julian oscillation. Geosci Lett 3:34. https://doi.org/10.1186/s40562-016-0066-z

Wheeler M, Kiladis GN (1999) Convectively coupled equatorial waves: analysis of clouds and temperature in the wavenumber–frequency domain. J Atmos Sci 56:374–399

Yang G-Y, Hoskins B, Slingo J (2007) Convectively coupled equatorial waves. Part I: Horizontal and vertical structures. J Atmos Sci 64:3406–3423. https://doi.org/10.1175/jas4017.1

Zhang C (2005) Madden–Julian oscillation. Rev Geophys 43:1–36

Zhang C, Ling J (2017) Barrier effect of the Indo-Pacific Maritime continent on the MJO: perspectives from tracking MJO precipitation. J Clim 30:3439–3459. https://doi.org/10.1175/jcli-d-16-0614.1